Accepted manuscript of: Lere-Adams, A.J., M.C. Dixon Wilkins, D. Bollinger, S. Stariha, R. Farzana, P. Dayal, D.J. Gregg, S. Chong, B.J. Riley, Z.M. Heiden, and J.S. McCloy, "Glass-bonded ceramic waste forms for immobilization of radioiodine from caustic scrubber wastes," *Journal of Nuclear Materials*, 591, 154938 (2024). https://doi.org/10.1016/j.jnucmat.2024.154938, PNNL-SA-192252

Glass-bonded ceramic waste forms for immobilization of radioiodine from caustic scrubber wastes

Arumala J. Lere-Adams,[1] Malin C. Dixon Wilkins,[1] David Bollinger,[1] Sarah Stariha,[3] Rifat Farzana,[4] Pranesh Dayal,[4] Daniel J. Gregg,[4] Saehwa Chong,[2] Brian J. Riley,[2] Zachariah M. Heiden,[5] John S. McCloy[1,2 *]

[1]School of Mechanical and Materials Engineering, Washington State University, Pullman, WA 99164, USA

[2]Pacific Northwest National Laboratory, Richland, WA 99354, USA

[3]Argonne National Laboratory, Lemont, IL 60439, USA

[4]Australian Nuclear Science and Technology Organisation, Lucas Heights, NSW 2234, Australia

[5]Nuclear Science Center, Washington State University, Pullman, WA 99164, USA

Abstract:

Glass-bonded sodalite composite waste forms have been developed for the immobilization of liquid radioactive wastes resulting from off-gas treatment during aqueous reprocessing of used nuclear fuel, with a particular focus on ^{129}I. The proposed composite waste form is comprised of aluminosilicate ceramic phases containing volatile radionuclides bonded with a glassy matrix. In this work, a suite of ten candidate low-temperature glass binders (ZnO-Bi_2O_3-based glasses and a Na_2O-B_2O_3-SiO_2 glass) were examined. Six glasses were mixed with caustic scrubber waste simulant previously converted into a sodalite-rich material (to provide glass fractions of 10 and 20 wt.%), uniaxially pressed into pellets, and sintered at 350 °C or 550 °C for 8 h in air. Iodine retention after heat treatment was assessed by neutron activation analysis, showing retention of 67-100% of expected iodine. The aqueous durabilities of the resulting materials were then determined, following the ASTM C1308 standard test, showing iodine releases of 1 to 23 $g \cdot m^{-2}$ after 4 d. The cumulative iodine release for the best performing system (a zinc-bismuth-borate glass binder) was <1 $g \cdot m^{-2}$, and its iodine retention from processing was 67%. The iodine releases compared favorably with other waste forms. In parallel, this best-performing composition was also consolidated *via* hot isostatic pressing (HIP) in a stainless-steel canister at 550 °C for 2 h under 100 MPa pressure. The HIPed sample was produced at the ~20 g scale and showed improved densification and minimal reaction with the canister.

Keywords: iodine; glass-bonded waste forms; chemical durability; bismuth; neutron activation analysis

*john.mccloy@wsu.edu (corresponding author)

Accepted manuscript of: Lere-Adams, A.J., M.C. Dixon Wilkins, D. Bollinger, S. Stariha, R. Farzana, P. Dayal, D.J. Gregg, S. Chong, B.J. Riley, Z.M. Heiden, and J.S. McCloy, "Glass-bonded ceramic waste forms for immobilization of radioiodine from caustic scrubber wastes," *Journal of Nuclear Materials*, 591, 154938 (2024). https://doi.org/10.1016/j.jnucmat.2024.154938, PNNL-SA-192252

1 Introduction and Background

1.1 Context

The generation of power by nuclear fission produces fission and activation products. The US Department of Energy (DOE) continues to research potential pathways for the reprocessing of used nuclear fuel (UNF) to close the nuclear fuel cycle in the US. One pathway for recycling uranium from oxide-based UNF involves aqueous reprocessing [1]. The volatile fission products evolved during fuel dissolution are captured by an off-gas system. Due to their gaseous nature, they tend to be more challenging to efficiently control compared to radionuclides that remain with solid or liquid phases during reprocessing operations. Unless correctly managed, these radionuclides will be released to the environment.

Any future UNF reprocessing facilities in the U.S. will be required to meet licensing requirements regarding volatile radionuclide capture [2]. The four volatile radionuclides restricted by the release limits governed by the US regulations are ^{3}H, ^{14}C, ^{85}Kr, and ^{129}I (40 CFR 190 - see supplementary information, SI), but ^{129}I will require the greatest degree of abatement [1]. With a half-life of 1.57×10^{7} years, ^{129}I is a significant contributor to the long-term dose in most geologic repository scenarios under consideration. Several proposals have been made for immobilizing ^{129}I to meet the necessary U.S. regulatory decontamination factors (DF) [3], defined as DF = 1 / [1 – efficiency (mass fraction)]. For example, if a solid sorbent bed is 99.9% efficient (0.1% is not captured), the DF would be 1000.

1.2 Caustic Scrubber

One potential flowsheet to meet the DF goals involves the use of an aqueous or molten-salt-based acidic or caustic scrubber (CS), followed by chemisorption on Ag-coated or Ag-impregnated adsorbents. These processes (especially CS) do not selectively trap iodine only, but also capture other halogen-bearing components (known as “tramp halogens”) and ^{14}C that could be present in the off-gas streams, thereby complicating further treatment of these streams for disposal [2]. The approximate composition of a used CS solution is [4]: 0.2 M NaOH, 0.03 M NaI, 0.1 M NaCl, 0.1 M NaBr, 0.6 M Na_2CO_3, 0.06 M $NaNO_2$, and 0.03 M $NaNO_3$. The I^-, Br^-, and ^{14}C (as $^{14}CO_3^{2-}$) are captured fission products whereas Cl^-, NO_2^- and NO_3^- come from the acidic solution used for fuel dissolution in the aqueous reprocessing scheme [5]. The two most promising solid sorbents currently in the advanced stages of testing in the U.S. are Ag-mordenite (AgZ) and Ag-functionalized silica aerogel (AgAero); both use Ag to chemisorb iodine, forming chemically durable AgI [6].

After full decontamination, a CS waste stream (one of two generated streams)—rich in Na^+, OH^-, halides (including ^{129}I), NO_x, and $^{14}CO_3^{2-}$—would be generated and require treatment and immobilization in tailored waste form processes. The other generated waste stream would be comprised of the AgI-containing solid sorbents [7, 8]. It is undesirable, though feasible [7, 9], to directly take the Ag-loaded solid

sorbent and make a waste form, since disposal of Ag in the U.S. is controlled by the Environmental Protection Agency under the Resource Conservation and Recovery Act (RCRA). Thus, one option to avoid this would be to elute the iodine from the Ag solid sorbent and immobilize it in a waste form free of Ag or combine it with the CS solution. A waste form pathway for this stream has recently been proposed [10].

1.3 Sodalite

Significant previous work exists investigating the feasibility of using sodalite as a potential waste form for immobilization of high iodine-content wastes. All of the anions in the CS (iodide, chloride, bromide, hydroxide, nitrate, nitrite, carbonate) have been previously shown to be accommodated within the sodalite and/or cancrinite structures [3, 11]. Briefly, the sodalite structure, nominally $Na_8(AlSiO_4)_6X_2$ with X being a monovalent anion, consists of 4- and 6-membered rings of AlO_4 and SiO_4 tetrahedra, connecting to form 'β-cages', within which various anions can be incorporated [3, 11]. The cancrinite structure is somewhat more complex, with larger cavities, notably a channel surrounded by 12-membered rings of AlO_4 and SiO_4 tetrahedra, although it also contains 6- and 4-membered rings [12]. Both structures can accommodate the same anions (*e.g.*, I^-, Cl^-, OH^-, CO_3^{2-}, SO_4^{2-}) with the preferred structure depending on the alkali and alkaline earth metals present, the Al/Si molar ratio, and the amount of water, though they are frequently observed crystallizing together in experimental studies [11, 13-15]. Sodalite structures often age into cancrinite structures over extended time in high pH conditions [16], such as in the case of sodalites from the bauxite residue from aluminum processing (see SI for more information).

1.4 Waste Form

The hot isostatic press (HIP) process has been long-considered as a viable technique for the processing of nuclear waste into durable waste forms [17]. The technology is maturing at the Australian Nuclear Science and Technology Organisation (ANSTO) through the construction and commissioning of a first-of-a-kind Synroc Waste Treatment Facility for the HIP treatment of ANSTO's intermediate-level liquid waste produced as a byproduct of radiopharmaceutical production [17, 18]. The scalability of the nuclear HIP process has also been demonstrated up to 100 kg [19]. The HIP canister requires sealing of well-packed powders with no low-temperature outgassing, so pre-calcination is often needed prior to loading samples into the canister and sealing it. Due to the application of high applied pressures during HIP processing, improved material densification is possible at lower temperatures than pressureless sintering [20].

As the materials to be processed are sealed within a canister (usually stainless-steel) prior to being pressed, another important advantage of HIP is that no volatiles are lost during processing as long as the canister remains intact. This is particularly important in the current work, given that the target was to immobilize iodine within the waste form and to prevent further iodine release during the consolidation process. HIP-processed Ag-iodosodalite waste forms have been previously demonstrated, with precursors

of Ag-exchanged zeolites [21-26], AgI + heat-treated zeolite A [27], or AgI + sol-gel $AgAlSiO_4$ (made from metal nitrates and colloidal SiO_2) [28]. A HIP of glass-bonded Na-iodosodalite waste forms has also been investigated [20], showing that glass-bonding improves densification and chemical durability. In the current study, HIP consolidation of a glass-bonded sodalite composite was demonstrated at the ~20 g scale and the resulting material was characterized.

In the current work, the immobilization of a simulant CS solution in a glass-bonded composite of cancrinite/sodalite is described, obtained by both sintering and HIP. The synthesis of the iodine-containing ceramic component was accomplished by a low-temperature (150 °C) processes, as described previously [29, 30]. For glass binders, chemically durable borosilicate or zinc-bismuth oxide glasses with low melting were utilized [31]. Considerations for selection of a specific glass binder include thermal stability, viscosity, and the availability of commercial compositions [32]. Sintered pellets were investigated with X-ray diffraction (XRD), density measurements, microscopic and chemical microanalysis, and chemical durability testing (ASTM 1308 method), and the iodine content was confirmed using neutron activation analysis (NAA). To assess the effect of the consolidation process, a further pair of otherwise identical samples were produced by pressureless sintering and by HIP, and the microstructural and phase results compared.

2 Methods

2.1 Sintering study

The converted sodalite (caustic scrubber) material utilized here was produced following the methods described by Bollinger et al. [30]. Briefly, aqueous and hydrothermal procedures were employed to synthesize a mixed sodalite (SOD) solid material from kaolinite and a CS solution simulant containing hydroxide, carbonate, chloride, bromide, and nonradioactive iodine. Experimental parameters, including reaction time, temperature, and type of reaction vessel, were varied to maximize conversion of a kaolinite precursor into SOD and cancrinite (CAN) products, while incorporating the CS anions and minimizing the amorphous content of the final material. Two different batches of CS solid, referred to as CS15 and CS17a, were synthesized at 150 °C and dried at 105 °C in air, with CS15 being washed and CS17a being calcined at 550 °C in air as a post-processing step [30]. Samples CS15 and CS17a, which showed high total SOD contents with powder XRD analyses, were used for consolidation with glass binder materials (see Table S-1).

Previous work [31] investigated ten compositions in the $ZnO–Bi_2O_3–B_2O_3$ and corresponding $ZnO–Bi_2O_3–SiO_2$ glass families, which were synthesized using conventional melt-quench techniques. Bulk glass formability was identified in four glasses, and these compositions were selected for use in this work. Two

additional glasses, NBS-4 [20] and Ferro glass EG2922 [20], were chosen as comparable references due to their previous use as binders for SOD or other low-temperature phases. The Ferro glass is a commercially available $ZnO–Bi_2O_3–SiO_2$ glass, while NBS-4 is a multicomponent borosilicate glass different from the borate and silicate systems explored. Compositions are detailed in Table 1.

The CS simulant waste powder was intimately mixed with 10 wt.% or 20 wt.% of glass binders using a mortar and pestle. Approximately 1 g of each composition was pelletized in a uniaxial press for 2 min, resulting in 10-mm diameter pellets ~5 mm thick. As-pressed pellets were placed on alumina sintering plates in a furnace and heated at 10 °C min^{-1} to 350 °C or 550 °C, held at peak temperature for 8 h, and then furnace cooled. Sintering temperatures were selected based on proximity to the glass transition temperatures (T_g) previously established [31]. Two simulant waste powders (CS15 and CS17a) were each pressed in ratios of 1:9 and 2:8 glass:waste by mass with six selected glasses prior to down-select (detailed in Table 1).

The materials produced were characterized by powder XRD, and based on these results, six compositions were chosen for further testing. The main criterion for down-selection was the final phase fraction of SOD, with higher SOD fractions being more desirable. In down-selection, only CS17a was used, because the initial pellet results for both CS batches showed similar phases and concentrations, but the CS17a starting material was more crystalline and did not have a wash step; washing would produce secondary waste and is hence less desirable. Additionally, phases were similar for 10 wt.% and 20 wt.% trials. To closely examine the impact of the glass binder fraction, one system (ZBS-2, see Table 1) was sintered at both 10 wt.% and 20 wt.% binder fractions; all others used only 10 wt.% binder to maximize the final waste loading. Finally, the composition similar to Ferro was excluded in favor of using the commercial composition. This down-selection thus resulted in five different glass compositions (five with 10 wt.%, one with 20 wt.%) and one CS powder lot. For the six down-selected compositions (Table 1), four identical pellets were synthesized for each one, to allow for a sufficient quantity of material for all characterization methods.

2.2 Hot Isostatic Pressing (HIPing) study

The converted sodalite CS17a, and $25ZnO–15Bi_2O_3–60B_2O_3$ glass (mol%) were utilized for HIP consolidation at ANSTO. To remove bound water, CS17a was calcined under an argon atmosphere at 600 °C for 14 h prior to HIPing. This re-calcined CS17a material was then mixed with 10 wt.% of $ZnO-Bi_2O_3-B_2O_3$ glass and homogenized using a mortar and pestle. The homogenized CS17a and glass mixture (~20 g) was transferred to a stainless-steel HIP canister (un-HIPed volume: 21 cm^3). The HIP canister was evacuated and sealed and HIPed at 550 °C, under 100 MPa of pressure for 2 h using an AIP 6-30H HIP.

Table 1. Compositional information of simulant CS wastes sintered with 10 wt.% or 20 wt.% of different glass compositions, including glass binder compositions, sintering temperatures (T_s), wt.% binder.

Down-selected	Ref #	Glass Composition in mol% [31]	T_s (°C)	Consolidation technique	Glass binder (wt.%)	CS-batch
ZBB-1	G1	25 ZnO - 15 Bi_2O_3 - 60 B_2O_3	550	Sinter	10	17a
			550	Sinter	20	17a
			550	Sinter	10	15
			550	Sinter	20	15
			550	HIP (100 MPa)	10	17a
ZBS-2-10	G2-1	25 ZnO - 50Bi_2O_3 - 25SiO_2	350	Sinter	10	17a
ZBS-2-20	G2-2		350	Sinter	20	17a
			350	Sinter	10	15
			350	Sinter	20	15
	G3	50 ZnO - 20 Bi_2O_3 - 30 SiO_2	550	Sinter	10	17a
			550	Sinter	20	17a
			550	Sinter	10	15
			550	Sinter	20	15
Ferro	G6A	49.7 ZnO - 18.9 Bi_2O_3 - 31.3 SiO_2 (Ferro glass- EG 2922)	550	Sinter	10	17a
	G6		350	Sinter	10	17a
			350	Sinter	10	15
			350	Sinter	20	15
ZBB-4	G4	25 ZnO - 50 Bi_2O_3 - 25 B_2O_3	350	Sinter	10	17a
			350	Sinter	20	17a
			350	Sinter	10	15
			350	Sinter	20	15
NBS-4	G5	62 SiO_2 - 8.16 B_2O_3 - 20.59 Na_2O – 3.72 Al_2O_3 – 4.50 CaO – 1.03 ZrO_2 (NBS-4) [32]	550	Sinter	10	17a
			550	Sinter	20	17a
			550	Sinter	10	15
			550	Sinter	20	15

2.3 Waste Form Characterization

The phases present in the produced materials were investigated by powder X-ray diffraction (XRD), utilizing a Panalytical X'pert Pro diffractometer with Ni-filtered Cu Kα radiation. Diffraction patterns were collected over the range 10° to 140° 2θ, step size 0.0084° 2θ and 0.228 s per step (109.2 s per degree 2θ); high count intensity was obtained for each sample to perform more accurate Rietveld refinement. The crystalline phases present were analyzed by matching the observed reflections to phases in the ICSD database. To quantify the relative fractions of the crystalline phases, Rietveld method refinements were performed in the HighScore Plus software package. Due to ambiguities in identifying the specific sodalite structure present (*i.e.,* which species is held within the sodalite cage), systems were compared using a sum of any fit sodalite phases. Other phases identified were nepheline, cancrinite, and quartz in some cases. The contribution of any amorphous fraction was neglected in all cases.

Backscatter electron (BSE) micrographs were collected with a JEOL JSM-7001F field emission gun scanning electron microscope (SEM). Materials were prepared by vacuum-impregnation with resin, before being polished with increasingly fine grades of glycol-based diamond suspensions down to a 0.25-µm

finish. Prior to imaging, samples were sputter coated with Pt to prevent sample charge build-up. Compositional information was obtained from energy dispersive X-ray spectroscopy (EDS), with data collected using a Bruker xFlash 6|60 silicon drift detector (SDD).

Pellet densities were measured by two different methods in order to quantify the relative porosities of the sintered materials. Bulk pycnometric densities ($\rho_{b,p}$) were measured using a Micromeritics AccuPyc II 1340 He gas pycnometer. Sample masses were accurately measured, and ten volume measurements performed, with the average value utilized to calculate $\rho_{b,p}$. Archimedes' method was also used to measure bulk Archimedes densities (ρ_a) and apparent open porosity (ϕ_a). Specimen masses were measured dry (m_{dry}), before submerging in absolute ethanol under vacuum, removing air from the open porosity. The submerged masses (m_{sub}) were measured, then the specimens were removed from the ethanol and excess ethanol was removed from the surfaces by setting samples onto an ethanol-saturated alumina disc. The masses of the pellets saturated with ethanol were then measured (m_{sat}). The temperature of the ethanol was monitored (to account for variations in liquid density, ρ_{EtOH}, as a function of temperature) and used alongside the measured masses to calculate the ρ_a using Equation 1 and the corresponding ϕ_a values using Equation 2.

$$\rho_a = (m_{dry} * \rho_{EtOH}) / (m_{sat} - m_{sub}) \quad (1)$$

$$\phi_a = (m_{sat} - m_{dry}) / (m_{sat} - m_{sub}) \quad (2)$$

At ANSTO, XRD patterns were obtained using a Panalytical Xpert-pro diffractometer system, (Almelo, the Netherlands) with Cu Kα radiation, angular range 5° − 80° 2θ, step size 0.05° 2θ, and scan step time of 3.17 s per step. Phase analysis was undertaken using the HighScore Plus software package. The bulk density and apparent porosity of the samples were determined according to ISO 18754 – 2020, (Method A: Determination of bulk density, apparent solid density and apparent porosity by liquid displacement, i.e., Archimedes' method). SEM-EDS was conducted using a Zeiss Ultra Plus SEM (Carl Zeiss NTS GmbH, Oberkochen, Germany), operating at 15 kV, equipped with an X-Max 80 mm^2 SDD X-ray microanalysis system (Oxford Instruments, Abington, Oxfordshire, UK). Samples were polished up to 1 µm diamond finish, carbon coated by sputtering and used for SEM-EDS analysis. Thermogravimetric analysis (TGA) along with evolved gas analysis (EGA) was conducted using a mass spectrometer (403 Aëolos® Quadro) coupled to the TGA (NETZSCH model STA 449 F3 Jupiter apparatus).

To determine the iodine concentration in the glass-bonded ceramic waste forms, neutron activation analysis (NAA) was performed. Six waste forms plus the powder CS material (CS17a) were irradiated along with potassium iodide standards for calibration. Vials containing the samples were irradiated at the Washington State University TRIGA reactor for 60 seconds at 10 kW (thermal flux = 6.89×10^{12} neutrons/cm^2 sec^{-1} and epithermal neutron flux = 1.35×10^{11} neutrons/cm^2 sec^{-1} at 1 MW). Irradiations at higher power or longer durations resulted in samples that exhibited too high of an activity to safely measure

before the ^{128}I had decayed (due to ^{24}Na, ^{80}Br, and ^{82}Br). Upon removal from the nuclear reactor, the samples were cooled for ten minutes then repackaged and measured with HPGe ORTEC gamma spectrometers for 15 minutes each. Data on the first samples were collected about 20 minutes after the end of the irradiation. The gamma peak for ^{128}I (443 keV) can be seen for about three hours post-irradiation, allowing for each sample to be measured twice and an average activity value of the two data collections is reported. Iodine weight percent was determined by plotting the measured activity of the potassium iodide calibration standards (μCi) as a function of iodine concentration. The resulting equation was used to determine the mass of iodine in the unknown samples, which was divided by the total mass to obtain the reported iodine concentrations. More detailed procedures as well as the gamma spectra are provided in the SI.

2.4 Chemical durability

The dissolution behaviors of the six down-selected samples were evaluated using a modified ASTM C1308 test procedure [33] at Argonne National Laboratory. For these tests, two specimens of each sample were prepared under the same conditions, one cylindrical and one quadrant, with the aim of examining the impact of different surface-to-volume (S/V) ratios during the testing procedure (see SI for more information). All experiments were conducted at 90 °C in Savillex jars (Eden Prairie, MN) in the same convection oven. The S/V ratios were 80 m^{-1} for the whole pellets and 8 m^{-1} for the quadrants and were controlled by varying the amount of the demineralized water leachant. In accordance with ASTM C1308, the surface areas of the pellets were determined geometrically, and did not account for any porosity intersecting the surface.

At each testing timepoint, the vessels were removed from the oven and solutions were removed for analysis. and the monoliths were returned to the vessels with fresh 18 MΩ demineralized water. The entire leachate volume was replaced every 24 h, and the vessels were returned to the oven, for 4 consecutive days. Dissolution is expected to occur at the kinetically limited rate at the test conditions of 90 °C in demineralized water (at approximately pH 6) without significant attenuation due to solution feedback or surface layer formation. on four consecutive days.

The incremental normalized mass loss, $NL_{i,n}$ (g m^{-2}), for each test interval was calculated using Equation (3), where $C_{i,n}$ is the concentration of species i measured in the test solution during the n-th test interval, S is the geometric surface area of the specimen as determined by measured dimensions, V is the volume of solution, and f_i is the mass fraction of the i-th species in the test specimen. The cumulative dissolution over a series of n-test intervals, $NL_{i,c}$ (g m^{-2}), was calculated as the sum of incremental $NL_{i,n}$ values over the timescale examined. NL was determined for Si, Na, I, and Zn as these were the most prevalent species in both binder and waste stream. From these calculations, cumulative releases for each element "i" ($NL_{i,c}$) can be calculated and plotted against the time scale to find leaching rates. The concentrations of elements used

for normalization were obtained from EDS measurements of the sample surfaces prior to leaching. The elemental mass fractions based on the most prevalent species in both binder and waste stream are listed in Table 2, as determined from large area averaged EDS.

$$NL_{i,\,n} = \frac{C_{i,n}}{(S/V) f_i} \tag{3}$$

The test solutions were analyzed to assess the extent of dissolution of each material during each test interval. The concentration of elements in the leachate solutions were measured using a PerkinElmer NexION 2000 inductively coupled plasma mass spectrometer (ICP-MS) calibrated with standards prepared from the National Institute of Standards and Technology (NIST) traceable solutions.

The kinetic dissolution rate (i.e., with negligible attenuation due to solution feedback or surface alteration layers) and extent of dissolution were assessed based on the cumulative release of key constituents. Cumulative *NL*(i) values corresponding to the sequential test intervals in ASTM C1308 tests are calculated as

$$\text{Cumulative } NL(i) = \sum_{j=1}^{4} NL(i)_j \tag{4}$$

$$NL(i) = \frac{m(i)}{S\, f(i)} = \frac{C(i)\, V}{S\, f(i)} \tag{5}$$

where *NL(i)* is the normalized mass loss based on species *i*, *m*(*i*) is the mass of element *i* released into solution, *S* is the glass surface area, and *f*(*i*) is the gross mass fraction of element *i* in the material, and *j* is an index for the interval. It is important to recognize that the plotted cumulative *NL*(i) values do not represent the cumulative releases of elements because the solution was replaced for each interval to minimize solution saturation effects. Instead, the cumulative values only indicate the consistency of the dissolution rate in sequential intervals. More details on the procedure and calculation are provided in the SI.

Table 2. Element mass fractions used to calculate *NL*(i).

Sample	I	Na	Si	Zn
ZBB-1	0.13	16	10	1.3
ZBS-2-10	0.09	16	11	0.25
ZBS-2-20	0.17	17	11	0.84
ZBB-4	0.12	16	11	0.27
NBS-4	0.06	15	12	0
Ferro	0.15	16	11	0.43

Accepted manuscript of: Lere-Adams, A.J., M.C. Dixon Wilkins, D. Bollinger, S. Stariha, R. Farzana, P. Dayal, D.J. Gregg, S. Chong, B.J. Riley, Z.M. Heiden, and J.S. McCloy, "Glass-bonded ceramic waste forms for immobilization of radioiodine from caustic scrubber wastes," *Journal of Nuclear Materials*, 591, 154938 (2024). https://doi.org/10.1016/j.jnucmat.2024.154938, PNNL-SA-192252

3 Results

3.1 Sintering matrix study

3.1.1 Diffraction

The two simulant waste powders (CS15 and CS17a) were each pressed with six selected glasses in glass:waste ratios of 1:9 and 2:8 (Table 1); a total of 24 pellets were pressed and sintered at either 350 °C or 550 °C, of which six compositions were down-selected as described previously. Analysis of the XRD patterns showed that significant fractions of the initial sodalite and/or amorphous content transformed into a nepheline phase for samples heat treated at 550 °C. This was more significant in waste forms with CS17a compositions compared to the analogous CS15 compositions. This may be a result of the additional calcining step performed during synthesis of CS17a, with nepheline formation initiating during this calcination.

After compositional down-selection, further samples of the six chosen compositions were produced by the same route for further characterization. High resolution XRD measurements were obtained on these materials for crystalline phase quantification. The fitting procedures for each phase was performed by consistently using the same starting structural models (phase files) across each composition. Table 3 provides a summary of the as-refined crystalline phase fractions, with SOD dominating across compositions G2-G6, with varying amounts of secondary phases, including cancrinite (CAN) and quartz (QTZ), also observed. Note that phases used in the refinement are listed in Table S-4. Sodalite in these compositions was determined as a total sodalite fraction including iodosodalite and anion-exchanged sodalite variants. A significant decrease was observed for the SOD fraction in Ferro glass after sintering at 550 °C (Ferro) compared to 350 °C (G6), with corresponding increase in nepheline (NEPH) formation. About 6.2 wt.% in total of bismuth silicate (BSO) phases were observed in Ferro after sintering at 550 °C. It is noteworthy that NBS-4 is a sodium borosilicate (a multicomponent glass including Al, Ca and Zr) glass-bonded pellet, and unlike other samples processed at 550 °C, it did not form NEPH.

Table 3. Summary of as-refined crystalline phase abundances (wt.%), with errors, of pellets comprised of simulant caustic scrubber waste (all CS17a) and different glass phases.

Pellet ID	Sintering Temp(°C)	Glass:CS	SOD	NEPH	CAN	QTZ	BSO	SUM
ZBB-1	550	1:9	57.2(4)	42.8(4)				100.0
ZBS-2-10	350	1:9	87.5(5)		11.5(5)	0.9(2)		99.9
ZBS-2-20	350	2:8	91.9(7)		8.2(7)			100.1
ZBB-4	350	1:9	85.9(5)		13.8(5)	0.3(1)		100.0
NBS-4	550	1:9	89.5(5)		10.6(5)			100.1
Ferro	550	1:9	78.5(3)	14.7(1)		0.4(1)	$Bi_2Si_2O_5$ - 4.4(1) *BiSiO* - 1.8(1)	99.8

3.1.2 Density

Density measurements were utilized in conjunction with SEM micrographs to examine the apparent porosity of all sintered pellets. It was generally observed that ZBB and ZBS glass binders result in pellets with less porosity than NBS glass binders, though significant porosity was observed in all materials produced (see Table 4). The high values of open porosity for the pellets as determined from Archimedes method measurements, ϕ_a, is likely due to the high surface area to volume ratios of the pellets produced here (2 mm thick, 20 mm diameter).

Table 4. Densities and open porosity of as-sintered glass-bonded pellets comprising simulant caustic scrubber waste and various glasses. Porosity error from Archimedes based on analytical balance.

Pellet ID	$\rho_{b,p}$ (g·cm^{-3})	*Std dev* (g·cm^{-3})	ϕ_a (vol%)	*Error* (vol%)
ZBB-1	2.46	0.0105	53	0.09
ZBS-2-10	2.59	0.0065	48	0.14
ZBS-2-20	2.68	0.0051	46	0.09
ZBB-4	2.47	0.0041	53	0.11
NBS-4	2.52	0.0028	50	0.10
Ferro	2.62	0.0017	54	0.07

3.1.3 Microscopy and microanalysis

Analysis of SEM micrographs showed that materials were heterogeneous and porous in all cases (see Figure 1, with larger area micrographs shown in Figure S-6). EDS maps corresponding to the regions are shown in Figure S-7. The regions of brightest contrast features in the BSE micrographs of ZBB-1, ZBS-2-10 and ZBS-2-20 corresponded to regions of increased Bi and Zn concentration, with significantly lower abundances of Si, Al, and Na compared to the bulk, presumably due to unreacted binder glass. Ring-like features are visible in ZBB-1. Generally, brighter features in the BSE micrographs of all measured samples indicate dispersion of the high average atomic number glass binders in the aluminosilicate powders.

Electron microprobe was attempted to gain further insight into specific features in the microstructure. However, significant beam damage was noted, leading to low quantification totals. Lack of quantification for additional elements (e.g., halides, nitrogen from nitrate/nitrite, carbon from carbonate) may also contribute to the low totals. Additionally, some features were very small, and volumetric averaging lead to some uncertainties. Nonetheless, a few qualitative assessments can be made. The concentrations given below for I concentration in wt.% are based on averages of 3-11 points from EPMA. Numbers listed in the paragraph below correspond to labeled features in the images in Figure 1 which were probed with EPMA.

Zn-Bi-B oxide glasses: For ZBB-1, bright (in BSE micrographs) fragments are the unreacted Bi-Zn-B oxide glass (1); dark grey matrix (2) is largely Na-Al-Si-O with some I (~0.03 wt.%); the dark black spots are voids (3), which are surrounded by collections of brighter crystals (4) which contain Na-Al-Si-O as well as some Bi-Zn-B, suggesting infiltration and potential reaction of the glass with the aluminosilicates, but apparently with little to no I. For ZBB-4, which was processed at lower temperature with a higher Bi content glass, the bright fragments are Bi-Zn-B oxide glass (1), and the matrix (5) is Na-Al-Si oxide with a small amount of B and Bi and some I (~0.12 wt.%).

Zn-Bi-Si oxide glasses: For ZBS-2-10, the bright features (6) are Bi-Zn-Si oxide glass, with some infiltration of Na and B; the major matrix (2) is again essentially Na-Al-Si-O with some I (~0.08 wt.%), thus "fused aluminosilicates"; some brighter areas suggest reaction between the aluminosilicate and Bi glass, being enriched relative to the regular matrix in Bi, Zn, B, and Na, and depleted in Al and Si, but still having ~0.06 wt.% I. For ZBS-2-20, with a higher fraction of starting glass, the phases are similar. For Ferro, which has much higher ZnO than the other glasses, the Na-Al-Si-O phase (2) remains associated with the I (~0.02 – 0.07 wt.%), sometimes reacting with Bi but not with Zn; the other main phase (7) is a Bi-Zn-Si oxide with some Na, possibly depleted in Bi.

Na-B-Si oxide glasses: For NBS-4, the average atomic number of the aluminosilicate crystalline phases (2) and the glass (8) is very similar. However, the iodine appears to remain associated with the crystalline phases. EDS mapping suggests a partitioning of some crystals containing Ca, which is in this glass.

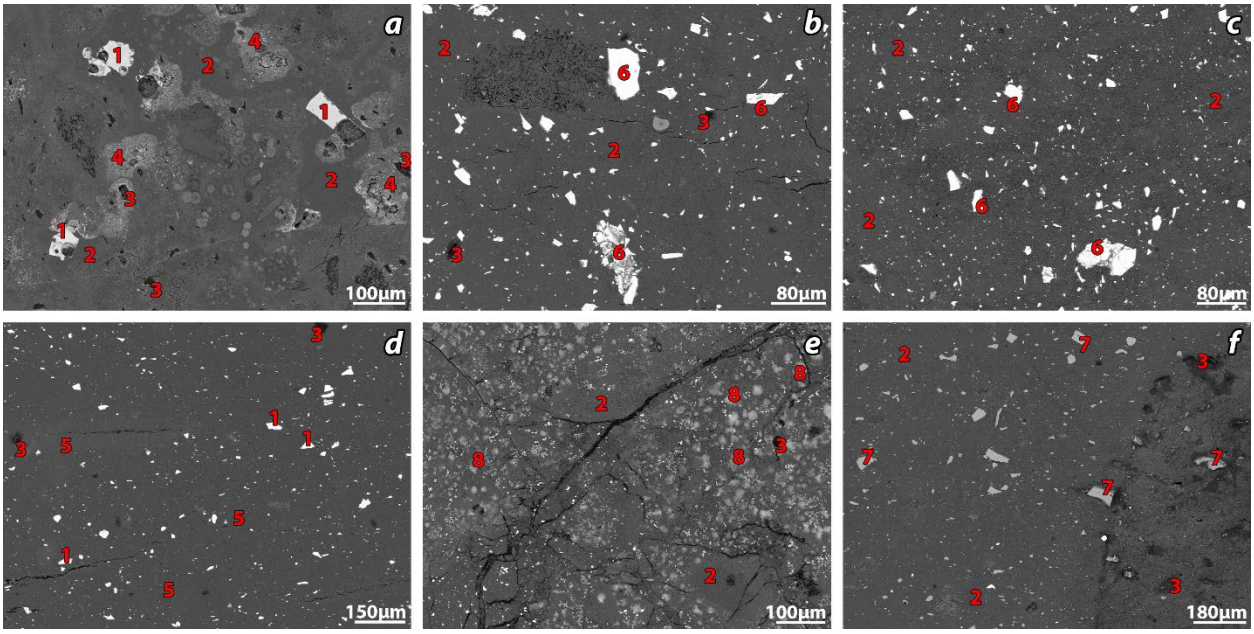

Figure 1: Back-scattered electron micrographs showing heterogeneous nature of the samples. (a) ZBB-1; (b) ZBS-2-10; (c) ZBS-2-20; (d) ZBB-4; (e) NBS-4; (f) Ferro

3.1.4 Neutron activation analysis (NAA)

Table 5 shows the determined iodine concentration from NAA, along with the estimated batched iodine and the calculated retention (measured/batched). The calculations for the estimated batch concentration are shown in the Table S-2. The initial CS powder showed slightly higher than 100% retention but was 100% within error. Other samples varied between 67% and 100% retention. There appears to be no correlation between processing temperatures 550 °C (ZBB-1, Ferro, NBS-4) or 350 °C (ZBS-2-10, ZBS-2-20, ZBB-4) as both groups have one sample at the lowest retention. Neither did it appear there was a correlation between chemistry (ZBB, ZBS including Ferro, NBS) and retention, other than the fact that the one NBS glass appeared to have ~100% iodine retention.

Table 5. Measured Iodine concentrations using potassium iodide calibration standards.

Composition	Sample Name	NAA measured iodine (wt.%)	Estimated batched iodine (wt.%)	Iodine retention after thermal treatment (%)
CS	C17a	0.21 ± 0.03	0.19	111 ± 16
ZBB-1	G1	0.12 ± 0.02	0.18	67 ± 11
ZBS-2-10	G21	0.13 ± 0.02	0.18	72 ± 11
ZBS-2-20	G22	0.11 ± 0.01	0.16	69 ± 6
Ferro	G6a	0.16 ± 0.03	0.19	84 ± 16
ZBB-4	G4	0.12 ± 0.01	0.18	67 ± 6
NBS-4	G5	0.18 ± 0.03	0.18	100 ± 17

3.1.5 Chemical durability testing

The semi-dynamic nature and short timescale of the modified ASTM C1308 test means that dissolution likely remained in a kinetic regime throughout. Surface microstructures of certain regions of the samples were examined by SEM before and after leaching. Both the matrix (grey regions) and inclusion phases (brighter regions) appear to show visible signs of surface leaching. Generally, all compositions showed some surface alteration as a result of the leaching process, *e.g.,* cracking seen in ZBS-2-10 and pitting observed in ZBB-1 and ZBS-2-20.

Normalized elemental mass losses of I, Na, Si, and Zn were calculated from the solution concentrations determined by ICP-MS and from EDS measurements on elemental concentration of the starting material. ASTM C1308 immersion tests are depicted as cumulative normalized loss ($NL_{i,c}$ for i-th constituent) versus reaction time (4 d) and these data are shown in Figure 2. The releases of Si and Na from all compositions studied here were of the same magnitude and showed near-linear behavior as a function of time. The releases of Zn were also near-linear with respect to time, although with some variations in magnitude depending on glass binder composition where Ferro had the highest release of Zn, while ZBB-1 and ZBS-2-20 had the lowest.

Overall, the cumulative mass losses of I ($NL_{I,c}$) varied in the tested samples from approximately 1 to 23 g m^{-2} over the leaching period. The lowest $NL_{I,c}$ value was for the boron-rich Zn-Bi oxide glass (ZBB-1), which had lower release than the Na-B-Si oxide glass (NBS-4) by a factor of 4.5 and showed marked increase over the four-day period. The most mass loss observed was with the ZBS-2-20, where pellets fell apart, and with Ferro glass (G6a), both Zn-Bi-silicate glasses. The Zn-Bi silicate glasses considered here are mechanically unstable. The lowest I release was seen for the B-rich binder ZBB-1 ($25ZnO\text{-}15Bi_2O_3\text{-}60B_2O_3$, mol%), with the highest releases observed for the Zn-Bi-Si binder ZBS-2-20, particularly composition ZBS-2-10 with 10 wt.% glass binder. The borate glasses were in general more chemically resistant to iodine release; however, Ferro glass (a silicate) showed the second lowest iodine release.

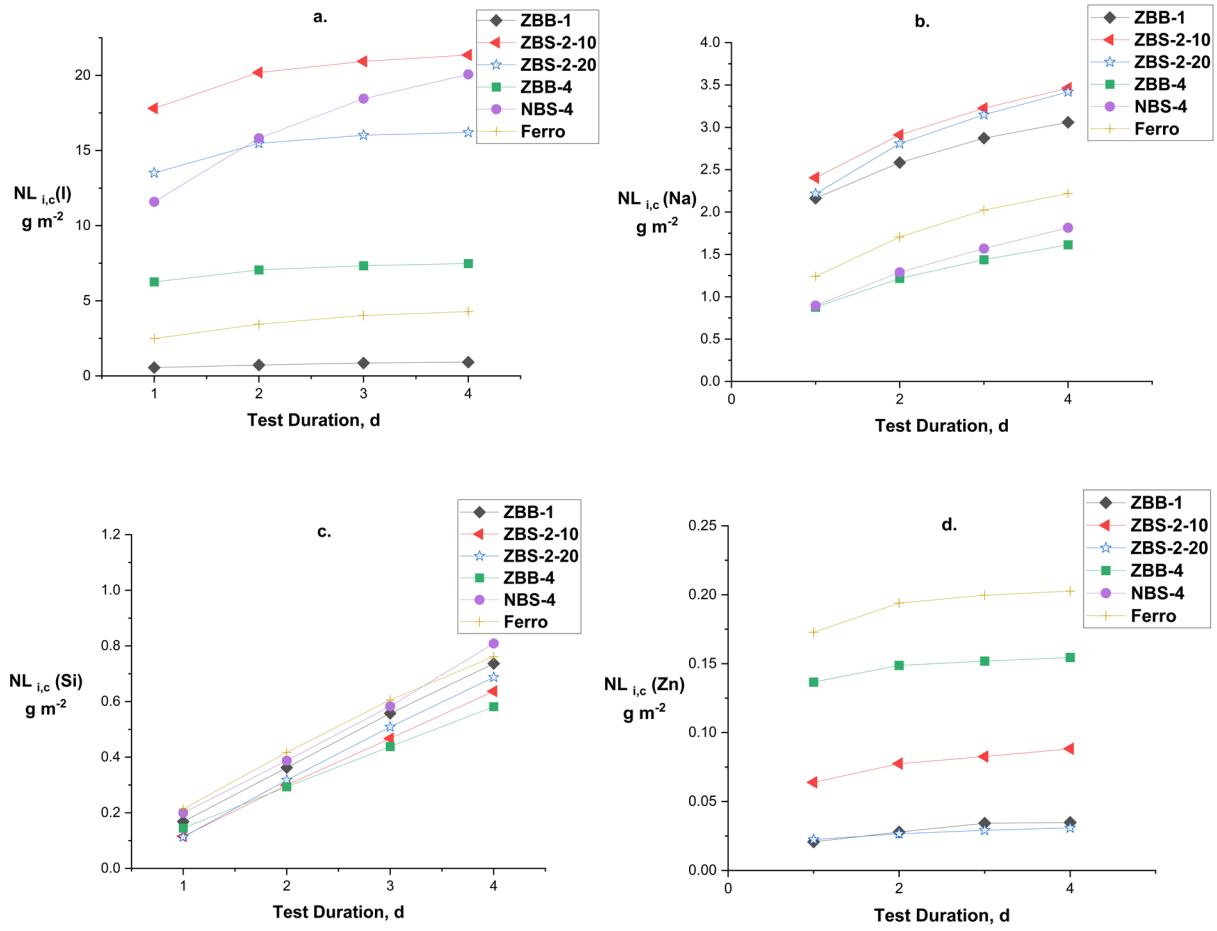

Figure 2. Cumulative normalized elemental releases of I, Na, Si and Zn (a, b, c & d) from simulant caustic scrubber waste bonded with different glass compositions, as-determined from ICP-MS. Pellets were leached following a modified ASTM C1308 methodology in deionized water.

SEM-EDS characterization of the surfaces before (Figure S-9) and after leaching (Figure S-10) provided additional comparative information, summarized as follows.

Zn-Bi-B oxide glasses: For ZBB-1, iodine and chlorine are well distributed across the surface both before and after leaching. For ZBB-4, the other borate glass, Bi, Zn, and Cl are spatially correlated. Iodine is well distributed but is enriched near Bi and Zn after leaching. Al and Na are correlated with each other in both glasses, before and after leaching. It is possible that the significant nepheline fraction present in glass ZBB-1 is beneficial towards I retention (e.g., the iodine was captured rather in the Bi-rich glassy phase), though other factors, including initial I content, true surface area, porosity, *etc.*, are also important contributors.

Bi-Zn-Si oxide glasses: For ZBS-2-10, Bi, Zn, and Cl are spatially coordinated. Iodine is well distributed, associated with all elements including Al and Na, which are themselves highly correlated. ZBS-2-20 is similar, but the Zn is somewhat less spatially correlated before leaching, but more so after leaching, again with Bi and Cl. Iodine is well distributed. For Ferro, Bi, Zn, Cl, and to a lesser extent I are correlated before leaching, whereas after leaching Zn has a much stronger correlation with Na and Al, and Bi and Cl have a strong association. Iodine remains dispersed before and after leaching.

Na-B-Si oxide glasses: For NBS-4, few changes are seen before versus after leaching. Both Cl and I remain well-dispersed in the matrix, and Na and Al are always strongly correlated.

3.2 HIPed matrix study

3.2.1 Powder calcination

The thermo-gravimetric analysis (TGA) of CS17a (Figure S-1) in an argon atmosphere showed a mass loss of approximately 2-3 wt.% up to 400 °C with a second mass loss of ~ 4-8 wt.% between ~700 – 1000 °C. This is in agreement with previous results published in the literature for this material *[30]*, with the mass loss from 700 °C attributed to sodalite cage breakdown releasing the cage anions *[30]*. The TGA data guided design of the HIP profile and a HIP consolidation temperature of 550 °C was chosen for the glass-bonded ceramic. Prior to HIPing at ANSTO, the as-supplied converted sodalite powder (CS17a) was re-calcined to remove bound water. Initially, re-calcination of a small sub-sample of CS17a (600 °C in air within a platinum crucible) was undertaken; however, this showed a net weight gain following the thermal treatment which was attributed to the intra-cage oxidation of nitrite sodalite (present in CS17a) to nitrate sodalite, as has been reported previously [34]. This was avoided by re-calcining the as-supplied CS17a powder under argon for 14 hours. The evolved gas analysis (EGA) data (Figure S-1) of the evolved gases during the re-calcination temperature profile (Figure S-1), indicated a minor and gradual release of water, CO_2 and NO. The mass loss at 800 °C appeared sharper and was associated with release of CO_2 and NO and subsequent breakdown of the sodalite/cancrinite cage structure.

The XRD patterns for the as supplied CS17a powder and the re-calcined material were nearly identical (see Figure S-2), with only a slight increase in the intensity of the major sodalite peaks and one additional minor peak of cancrinite (~28° 2θ) was observed. This could be attributed to a reduction of amorphous content and subsequent increase in the crystallinity of the mixed anion sodalite and cancrinite following the re-calcination process. Importantly, XRD analysis confirmed that there was no decomposition of the major sodalite phase following re-calcination in argon at 600 °C.

3.2.2 Glass-bonded sodalite composite

An identical glass to ZBB-1 (25ZnO-15Bi_2O_3-60B_2O_3, mol%) was produced at ANSTO at 1000°C using melt quench method, and the amorphous nature of the material was confirmed by XRD (see Figure S-3). Two broad humps were observed in the XRD pattern at around 30° 2θ and 50° 2θ as previously observed for similar ZnO-Bi_2O_3-B_2O_3 glass systems [35].

The XRD pattern of the HIPed glass-bonded sodalite composite waste form is shown in Figure 3. As previously discussed for the sintered sample (ZBB-1), XRD analysis of the HIPed sample showed sodalite as the major phase together with minor amounts of nepheline. For comparison, a pressed pellet was also sintered (550 °C for 2 h in argon) using the same powder mixture (i.e., re-calcined) used for HIP consolidation. The XRD pattern for the sintered composite showed lower intensity of the reflections at 2θ angles of ~21°, 27°, and 30°, which indicates a decrease in the nepheline phase abundance as compared to the HIPed sample. A Rietveld refinement assuming no amorphous component resulted in the following phases for the HIP (sintered) samples: sodalite 74.5% (91.0%), nepheline 24.5% (8.5%), SiO_2 1.0% (0.5%).

The addition of the glass phase to form a glass-bonded ceramic composite appears to destabilize sodalite in favor of nepheline at this consolidation temperature, and this is evident in the XRD pattern for both the sintered and HIPed sample. This formation of nepheline is not strictly a function of temperature, as shown in Figure S-4. A series of heat treatments were performed on CS17a powder alone at discrete temperatures between 350-900 °C. XRD observed nepheline formation with 900 °C heat treatment but not 750 °C, indicating that temperature alone cannot be responsible for nepheline formation, since it occurred at 550 °C in the glass-bonded samples in both sinter and HIP conditions.

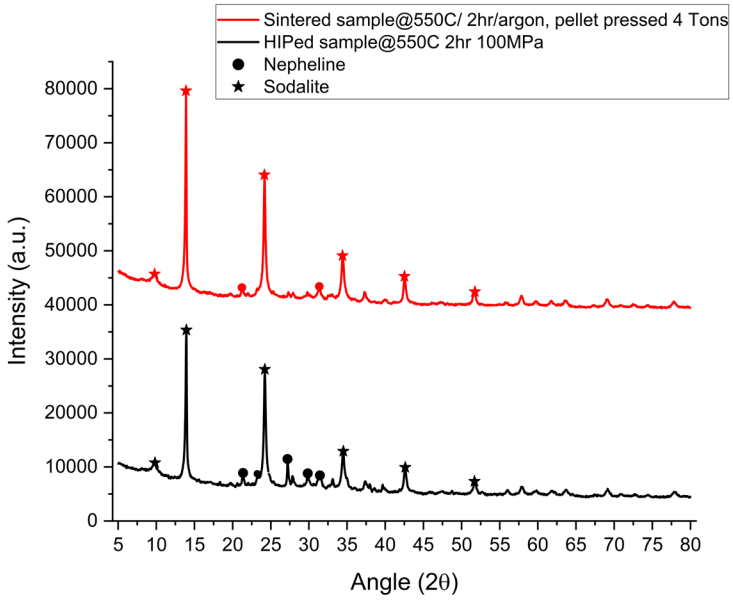

Figure 3. XRD pattern of the comparison between Sintered and HIPed glass-bonded ceramic waste form.

SEM micrographs of the HIPed waste form are shown in Figure 4. Although a re-polishing step was undertaken up to a 1-µm finish, the microporous structure of sodalite was maintained as the major phase in the SEM. The iodine content of these sodalite areas were measured by EDS to be 0.67 – 1.41 wt.% (noting that the EDS detector used was not capable of detecting B). The nominal composition of sodalite is ~$Na_8(AlSiO_4)_6X_y$ (assuming 8 cations for the Na site and X denotes the anions e.g., Cl^-, I^-) where y = 2. Minor amounts of Zn and Bi (~2.5 wt.%) were also evident in the EDS analyses of the sodalite phase and may be attributed to reaction/diffusion of the binder glass with the CS17a, or possibly due to the inclusion in the EDS analysis of nearby Zn/Bi rich grains. Within the sodalite matrix, brighter regions were dispersed, and these showed high Bi and Zn concentration, with lower abundances of Si, Al, and Na compared to the bulk sodalite (labeled as Bi-rich phase in Figure 4). The nominal composition of these regions resembles nepheline ~$NaAlSiO_4$ (assuming 1 cation for Na) without considering Bi and Zn (and B as the EDS detector used was not capable of detecting B) from the glass binder. The brightest contrast phase in the SEM of the HIPed sample was determined to be unreacted binder glass fraction and was in very low abundance (~1 – 2 vol.%). The particle size of the glass binder used in the HIP studies was selected to be < 45 µm, and only a few fragments were found intact with size ~ 2-40 µm.

These observations, together with the sodalite-type morphology of these bright areas in Figure 4, suggest the binder glass has reacted with sodalite to break down its cage structure with subsequent formation of nepheline and release of Na and I. This agrees with results from XRD analysis. Further, it is possible that during this reaction, the released Na and I is incorporated into the binder glass. In agreement with this hypothesis, it is observed that up to ~0.27 wt.% of I is found within the brighter glassy fragmented areas by

SEM-EDS analysis. As a result, although a fragment of the target I-bearing sodalite has been destabilized in this glass-bonded ceramic, the reaction has likely led to the incorporation of the I within the glass-binder and therefore may still provide a suitably chemically durable material for I immobilization. This would explain the relatively low release of I in the chemical durability tests for the sintered version (ZBB-1) of this material. The suitability of this glass system for I incorporation was also demonstrated *via* a recent study on the B_2O_3-Bi_2O_3 glass, which showed that iodine atoms tend to bond with bismuth atoms and improve the stability of I in the waste form [36]. Due to smaller grain size and porous nature of the sample, a further transmission electron microscopy (TEM) investigation is required to confirm these observations.

A comparative SEM image of the sintered sample (Figure S-8) showed an increased abundance of unreacted glass fragments compared to the HIPed sample, and this agrees with observations from XRD analysis, which suggested lower nepheline formation for the argon sintered sample relative the HIPed sample. However, the SEM of the sintered sample showed a higher abundance of pores/voids (dark areas) relative to the HIPed sample. The bulk density ($\rho_{b,p}$) and apparent porosity (ϕ_a) were measured for the sintered and HIPed sample and were determined to be $\rho_{b,p}$ = 1.25±0.06 g cm^{-3}, ϕ_a = 45±2 % and $\rho_{b,p}$ = 1.63±0.09 g cm^{-3}, ϕ_a = 21±10 %, respectively. The improved bulk density and lower apparent porosity of the HIPed sample agrees with the SEM results and demonstrates the advantage of HIPing over sintering for this material.

EDS analysis of the dark contrast areas labelled “amorphous phase” in the SEM image (see Figure 4) showed the presence of predominantly Na, Si, Al, along with Zn (0.23 wt.%) and I (~0.48 wt.%). The stoichiometry was close to sodalite. This area was attributed to an amorphous phase (without any grain boundary) present in the particle-particle interspaces of the HIPed waste form. A similar morphology was also observed in the sintered waste form (Figure S-8).

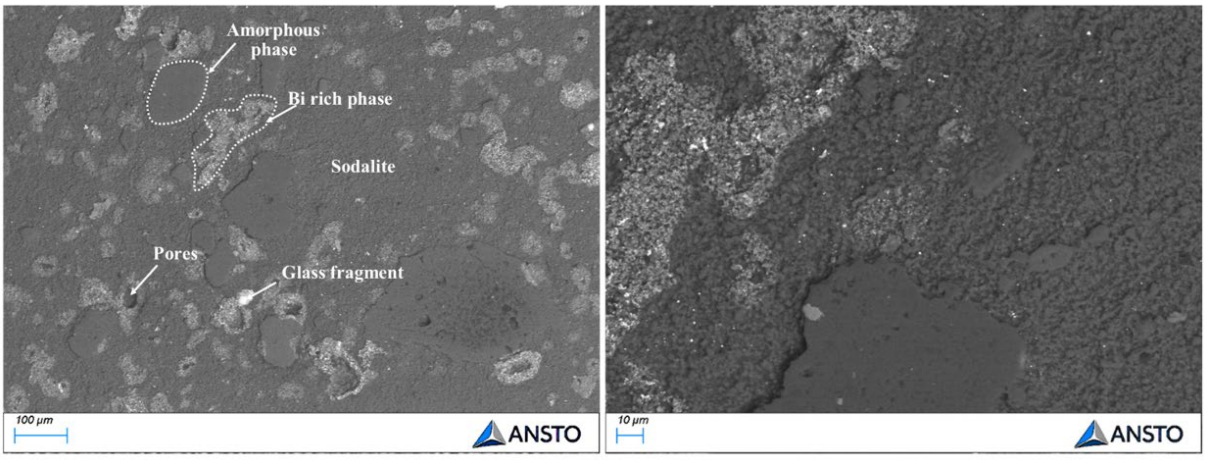

Figure 4. 100x (left) and 500x (right) magnifications for backscattered SEM images of the HIPed glass-bonded ceramic waste form

3.2.3 HIPed waste form-canister interaction zone

Previous studies have investigated the interaction of silver iodo-sodalite with the HIP canister at the interface between the HIP canister and the waste form [37, 38]. In general, sodalite was observed to be destabilized at the interface between the waste form and the HIP canister, resulting in the formation of nepheline and AgI, and in some cases an oxide layer was also formed. Although previous studies have considered the effect of different HIP canister materials on this interaction, they have all been undertaken at relatively higher temperature (≥ 750 °C) compared to the lower temperature employed in the current study. The bulk glass-bonded material in the current study showed a very similar morphology to that observed near the interface (Figure 5). Therefore the interaction zone shows no evidence for any elemental diffusion from the HIP canister, oxide layer formation, sodalite destabilization or phase alteration. The low temperature HIP consolidation coupled with the low melting glass binder provides an avenue to produce HIPed iodine bearing sodalite without occurance of any altered phase or elemental diffusion at the HIP canister – waste form interface.

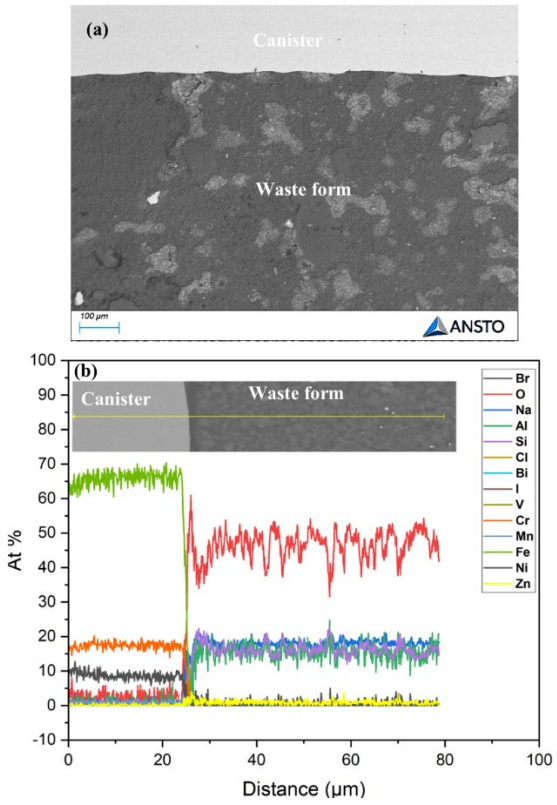

Figure 5. (a) Backscattered SEM image of the waste form – HIP canister interaction zone showing no oxide layer formation and (b) EDS line scan across the interface showing no evidence for elemental diffusion. In (b), the interface is at the ~20 µm mark, where the metal canister and the waste form materials meet, the distance 0-20 µm represents the distance from within the HIP canister towards the interface with the waste form, and 20-60 µm represents the distance from the interface towards the bulk waste form.

4 Discussion

ZBB-1, a boron-rich glass from the Zn-Bi-B oxide system, displayed the lowest normalized release of iodine after 4 days of leaching of the consolidated waste form (Figure 2a). This sample, sintered at 550 °C for 8 h, contained a significant fraction of nepheline formed from sodalite over the course of the heat treatment, but this appeared to be beneficial with respect to reducing iodine release, though further work examining the other factors that impact iodine release is necessary. The densities and porosities of all the sintered pellets produced in this study were of similar orders of magnitude, based on both pycnometry and Archimedes measurements. Future work may focus on improving the mechanical stability of the sintered materials, as significant optimization would be required to prevent cracking during characterization and leaching, in part due to the high porosities seen here. Normalized released rates in ASTM 1308 tests, per the test methodology, are calculated based on geometric surface areas, and not the true surface areas, which are quite large for these porous samples. Thus, if true surface areas were used to normalize the data, the elemental release rates could likely be much less in most cases.

In the starting CS material, the mass fraction of the iodine anion in the total starting aluminosilicate powder product was ~0.19 wt.% [30] (see also Table S-2), and the formation of sodalite phases across all samples show the potential for immobilizing the volatile anions from reprocessing. Nepheline forms in these Zn-Bi oxide glass waste forms when processed at higher temperatures (550°C), and nepheline has also been reported as a thermal phase transformation from chlorosodalite [39], although at 250-350°C higher than as observed here (i.e., 800-900 °C). In another study of thermal transformation of hydroxysodalite [40], water and cage hydroxide was removed by 350°C, maintaining the sodalite structure but with an empty cage; starting ~500°C, alpha carnegieite formed, with nepheline formation beginning ~700°C.

As briefly described previously, to investigate the effect of thermal treatment on the aluminosilicates without glass, CS17a was heat treated at select temperatures, then cooled and measured with XRD (Figure S-4). With heat treatment up to 400 °C, major sodalite, minor Na-exchange Zeolite E (known to transform on heating to sodalite [41]), and trace cancrinite are evidenced. At 550 °C the CS is essentially all sodalite, while between 750-900 °C, the system becomes ~1/3 carnegieite and ~2/3 nepheline. Apparently, then, in the presence of the Zn-Bi oxide binder glasses, nepheline can form at significantly lower temperatures (350°C < T < 550°C) in the case of the caustic scrubber aluminosilicates. The presence of nepheline and its correlation with lower cumulative loss of iodine in ZBB-1 and Ferro could be faciliting the binding of released iodine from sodalite cages to the bismuth-containing glass, as a strong correlation is observed here (EDS, see Figure S-9). Multiple recent studies also showed the role of bismuth oxide containing glasses as maintaining good stabilization of iodine [42, 43].

A further calcination of CS17a was undertaken at 600 °C for 14 h in argon atmosphere for the HIP sample to remove any potential bound water prior to HIP consolidation. This re-calcination step did not cause further nepheline formation as evidenced by comparison with the diffraction pattern of the heated CS17a alone (Figure S-2). However, the HIPed glass bonded sodalite composite showed increased nepheline formation with less porosity as observed in XRD and SEM results (Figure 3, Figure S-8). As dicussed for ZBB-1, nepheline formation is not detrimental towards I retention, as iodine potentially can be captured in the bright Bi-rich glassy phase. Mechanical stability of pellets remains to be optimized, as it was observed that HIPing leads to improved densification and differs in porosity from its sintered analogue by a factor of two.

For comparison with the current waste forms, a compilation of iodine release values from ASTM C1308 tests was produced (Table 6). Our study demonstrates comparably low iodine release in most cases with other waste forms at a similar initial iodine concentration for glass bonded and spark plasma sintered waste forms. Normalized release rates in this work are also in the observed regime of values from other studies, generally low for low starting iodine concentration and varying nonlinearly in other cases. Additionally, the waste forms demonstrated here have good iodine retention after thermal treatment, ≥67% iodine retention, in addition to low iodine release in the chemical durability test.

Table 6. Iodine waste form chemical durability (iodine release by ASTM C1308) in the current study compared to other iodine waste forms

Material[(a)]	Sample name[(b)]	Method[(c)]	Iodine conc. (mass%)	Cum. NL(I) (g/m^2)	NR(I) ($g/m^2/d$)	Reference
ZBB-1	G1	GB	0.12	0.92	7.70×10^{-1}	This work
ZBS-2-10	G21	GB	0.13	21.36	2.01×10^{2}	This work
ZBS-2-20	G22	GB	0.11	16.21	1.53×10^{2}	This work
Ferro	G6a	GB	0.16	4.28	3.56×10^{0}	This work
ZBB-4	G4	GB	0.12	7.48	7.03×10^{0}	This work
NBS-4	G5	GB	0.18	20.07	1.65×10^{1}	This work
Al-Si-xg	AgI-Xero-1	SPS	0.4	40.36	1.01×10^{1}	*
Al-Si-xg	AgI-Xero-2	SPS	0.4	66.76	1.67×10^{1}	*
Al-Si-xg	AgI-Xero-3	SPS	0.39	68.15	1.70×10^{1}	*
Al-Si-xg	AgI-Xero-4	SPS	0.21	0.04	9.54×10^{-3}	*
Al-Si-xg	AgI-Xero-5	SPS	0.28	0.04	1.11×10^{-2}	*
Al-Si-xg	AgI-Xero-6	SPS	0.31	0.04	1.01×10^{-2}	*
Al-Si-xg	AgI-Xero-7	SPS	0.31	0.04	9.66×10^{-3}	*
Al-Si-xg	AgI-Xero-8	SPS	0.3	0.03	7.35×10^{-3}	*
Al-Si-xg	AgI-Xero-9	SPS	0.3	0.01	1.72×10^{-3}	*
Al-Si-xg	AgI-Xero-10	SPS	0.29	0.03	6.36×10^{-3}	*
Al-Si-xg	AgI-Xero-11	SPS	0.27	0	6.05×10^{-4}	*
Ag-FAU	AgI-FAU-1	SPS	0.46	0.01	1.68×10^{-3}	#
Ag-FAU	AgI-FAU-2	SPS	0.46	0.01	1.47×10^{-3}	#
Ag-FAU	AgI-FAU-3	SPS	0.41	0.01	2.03×10^{-3}	#
Ag-FAU	AgI-FAU-4	SPS	0.43	0.01	1.61×10^{-3}	#
Ag-FAU	AgI-FAU-5	SPS	0.43	0.01	2.35×10^{-3}	#
Ag-MOR	AgI-MOR-1	SPS	0.18	2.94	7.35×10^{-1}	#
Ag-MOR	AgI-MOR-2	SPS	0.12	0.42	1.04×10^{-1}	#
Ag-MOR-HIP	HIP22-A	HIP	8.3	29.44	7.36×10^{0}	*
Ag-MOR-HIP	HIP22-B	HIP	7.8	63.51	1.59×10^{1}	*
Ag-MOR-HIP	HIP22-C	HIP	5.5	7.87	1.97×10^{0}	*
Al-Si-ag	LTE-2	LTE	38	30.73	7.68×10^{0}	*
Al-Si-ag	Aero22-4	SPS	4.6	2.59	6.50×10^{-1}	*
Al-Si-ag	Aero22-6	SPS	2.3	2.45	6.10×10^{-1}	*
Al-Si-ag	Aero22-7	SPS	11	1.06	2.60×10^{-1}	*

*These results were obtained by personal communication with Sarah Stariha, ANL, and are pending publication.
#Asmussen, R.M., A.L. Fujii Yamagata, J. Turner, J. Pauley. 2023. *Populating the Iodine Waste Form Degradation Model*. PNNL-SA-189128, Pacific Northwest National Laboratory, Richland, WA.
(a) Al-Si-xg denote aluminosilicate xerogel; Ag-FAU denotes silver faujasite zeolite; Ag-MOR denotes silver mordenite zeolite; Al-Si-ag denote aluminosilicate aerogel; Ag-MOR-HIP denotes silver mordenite zeolite HIPed in stainless steel can
(b) Description of original sample name
(c) GB denotes glass-bonded; SPS denotes spark plasma sintering; HIP denotes hot isostatic pressing; LTE denotes low temperature encapsulation method

5 Summary and Conclusions

In this work, low-temperature conditions for the mineralization of a simulant caustic scrubber waste and consolidation of this waste with glass binders was examined. Six glass binders, from the ZnO-Bi_2O_3-B_2O_3, ZnO-Bi_2O_3-SiO_2 and alkali aluminoborosilicate systems, were investigated for immobilizing the aluminosilicate waste powders, and sintered pellets utilizing these glass as low-fraction (10 or 20 wt.%) binders were produced for chemical durability testing. The boron-rich $25ZnO$-$15Bi_2O_3$-$60B_2O_3$ glass ZBB-1 was the most chemically durable with respect to I release over the four-day test period, where a cumulative

iodine release after four days was 0.92, corresponding to a rate of ~0.8 g m^{-2} d^{-1}. Overall, normalized iodine loss values were similar to comparable tests values from other waste form studies.

Additionally, a sample of the best composition was hot isostatically pressed inside a stainless-steel canister. The HIP also resulted in minor conversion of sodalite to nepheline but the HIPed samples had lower porosity than its sintered analogue. Consolidating the waste form within the stainless-steel HIP canisters and *via* the HIP process also ensures no iodine release. Though chemical durability tests were not conducted on the HIP sample, given the nature of the surface area normalization for the ASTM C1308 test, it is assumed that the HIP sample would have even lower iodine release than the sintered sample.

Although the starting amount of iodine in the waste form is only a small concentration, due to the presence of many other anions from the caustic scrubber solution, neutron activation analysis was able to successfully quantify iodine as 0.19 wt% in the CS (essentially 100% retention). Further, glass-bonding was conducted 350-550 °C, and neutron activation analysis confirmed ≥67% iodine retention after thermal treatment. In the future, to obtain a representative comparsion between our examined pelletized waste forms and real CS wastes, scale up of pellet size (and potentially initial iodine concentration) would be important factors to explore.

6 Acknowledgements

This work was supported by the US Department of Energy – Nuclear Energy University Program (NEUP), DE-NE0008964. We thank Dr. Tina Nenoff for providing some of the Ferro 2922 for our study. PNNL is operated by the Battelle Memorial Institute for the U.S. Department of Energy under contract DE-AC05-76RL01830. Argonne National Laboratory is operated by UChicago Argonne, LLC, under Contract DE-AC02-06CH11357. ANSTO co-authors would like to thank Christian Deura for HIPing, Iveta Kurlapski for assistance with sample preparation and Nuclear Science and Technology (NST) at ANSTO for material characterizations. We also thank Gavin McCloy for assistance with the NAA sample preparation.

7 REFERENCES

[1] J.D. Vienna, E.D. Collins, J.V. Crum, W.L. Ebert, S.M. Frank, T.G. Garn, D. Gombert, R. Jones, R.T. Jubin, V.C. Maio, J.C. Marra, J. Matyas, T.M. Nenoff, B.J. Riley, G.J. Sevigny, N.R. Soelberg, D.M. Strachan, P.K. Thallapally, and J.H. Westsik, Closed Fuel Cycle Waste Treatment Strategy, INL/EXT-15-34504, PNNL-24114, Idaho National Laboratory, Idaho Falls, ID (2015). https://doi.org/10.2172/1178373

[2] N.R. Soelberg, T.G. Garn, M.R. Greenhalgh, J.D. Law, R. Jubin, D.M. Strachan, and P.K. Thallapally, Radioactive Iodine and Krypton Control for Nuclear Fuel Reprocessing Facilities, Sci. Techn. Nucl. Install., 2013 (2013) 702496. http://dx.doi.org/10.1155/2013/702496

[3] B.J. Riley, J.D. Vienna, D.M. Strachan, J.S. McCloy, and J.L. Jerden Jr, Materials and processes for the effective capture and immobilization of radioiodine: A review, J. Nucl. Mater., 470 (2016) 307-326. http://dx.doi.org/10.1016/j.jnucmat.2015.11.038

[4] R.T. Jubin, Composition of caustic scrub solution, personal communication (2019).

[5] R.T. Jubin, Design and Test Plan for an Integrated Iodine Scrubber and Polishing Bed System, ORNL/SR-2017/564; NTRD-MRWFD-2018-000209, Oak Ridge National Laboratory, Oak Ridge, TN (2017). https://doi.org/10.2172/1490720

[6] R.T. Jubin, S.H. Bruffey, and J.A. Jordan, Testing of an Integrated Iodine Scrubber and Polishing Bed System, ORNL/TM-2018/1000; NTRD-MRWFD-2018-000195, Oak Ridge National Laboratory, Oak Ridge, TN (2018). https://doi.org/10.2172/1490720

[7] J. Matyáš, N. Canfield, S. Sulaiman, and M. Zumhoff, Silica-based waste form for immobilization of iodine from reprocessing plant off-gas streams, J. Nucl. Mater., 476 (2016) 255-261. https://doi.org/10.1016/j.jnucmat.2016.04.047

[8] C.W. Abney, Y. Nan, and L.L. Tavlarides, X-ray Absorption Spectroscopy Investigation of Iodine Capture by Silver-Exchanged Mordenite, Ind. Eng. Chem. Res., 56 (2017) 4837-4846. http://dx.doi.org/10.1021/acs.iecr.7b00233

[9] T.J. Garino, T.M. Nenoff, J.L. Krumhansl, and D.X. Rademacher, Development of waste forms for radioactive iodine, Ceram. Trans., 217 (2010) 35-42. https://doi.org/10.1002/9780470909874.ch5

[10] A. Yadav, S. Chong, B.J. Riley, J.S. McCloy, and A. Goel, Iodine Capture by Ag-Loaded Solid Sorbents Followed by Ag Recycling and Iodine Immobilization: An End-to-End Process, Ind. Eng. Chem. Res., 62 (2023) 3635-3646. https://doi.org/10.1021/acs.iecr.2c04357

[11] S. Chong, J. Peterson, J. Nam, B. Riley, and J. McCloy, Synthesis and characterization of iodosodalite, J. Am. Ceram. Soc., 100 (2017) 2273-2284. http://dx.doi.org/10.1111/jace.14772

[12] G.D. Gatta and P. Lotti, Cancrinite-group minerals: Crystal-chemical description and properties under non-ambient conditions—A review, Am. Miner., 101 (2016) 253-265. https://doi.org/10.2138/am-2016-5282

[13] W.A. Deer, R.A. Howie, and J. Zussman, Sodalite Group, In *An Introduction to Rock-Forming Minerals*, Addison-Wesley Longman, London, 316-351 (1992).

[14] A.R. Gerson and K. Zheng, Bayer process plant scale: transformation of sodalite to cancrinite, J. Cryst. Growth, 171 (1997) 209-218. http://dx.doi.org/10.1016/S0022-0248(96)00482-4

[15] Y. Deng, M. Flury, J.B. Harsh, A.R. Felmy, and O. Qafoku, Cancrinite and sodalite formation in the presence of cesium, potassium, magnesium, calcium and strontium in Hanford tank waste simulants, Appl. Geochem., 21 (2006) 2049-2063. http://dx.doi.org/10.1016/j.apgeochem.2006.06.019

[16] M.C. Barnes, J. Addai-Mensah, and A.R. Gerson, The mechanism of the sodalite-to-cancrinite phase transformation in synthetic spent Bayer liquor, Microp. Mesop. Mater., 31 (1999) 287-302. http://dx.doi.org/10.1016/S1387-1811(99)00079-7

[17] E.R. Vance, D.T. Chavara, and D.J. Gregg, Progress on Ongoing Waste form HIP projects at ANSTO, MRS Adv., 3 (2018) 1059-1064. https://doi.org/10.1557/adv.2018.328

[18] E.R. Vance, D.T. Chavara, and D.J. Gregg, Synroc development—Past and present applications, MRS Energy Sustain., 4 (2017) E8. https://doi.org/10.1557/mre.2017.9

[19] K.M. Goff, M.F. Simpson, K.J. Bateman, and D.W. Esh, Unirradiated testing of the demonstration-scale ceramic waste form at ANL-West, Trans. Amer. Nucl. Soc., 1997) 79-80.

[20] S. Chong, B.J. Riley, R.M. Asmussen, A.R. Lawter, S.H. Bruffey, J. Nam, J.S. McCloy, and J.V. Crum, Iodosodalite synthesis with hot isostatic pressing of precursors produced from aqueous and hydrothermal processes, J. Nucl. Mater., 538 (2020) 152222. https://doi.org/10.1016/j.jnucmat.2020.152222

[21] G.P. Sheppard, J.A. Hriljac, E.R. Maddrell, and N.C. Hyatt, Silver Zeolites: Iodide Occlusion and conversion to Sodalite – a potential ^{129}I waste form?, Mat. Res. Soc. Symp. Proc., 932 (2006). http://dx.doi.org/10.1557/PROC-932-36.1

[22] E.R. Maddrell, E.R. Vance, C. Grant, Z. Aly, A. Stopic, T. Palmer, J. Harrison, and D.J. Gregg, Silver iodide sodalite – Wasteform / Hip canister interactions and aqueous durability, J. Nucl. Mater., 517 (2019) 71-79. https://doi.org/10.1016/j.jnucmat.2019.02.002

[23] R.T. Jubin, S.H. Bruffey, and J.A. Jordan, Fundamental Aspects of Zeolite Waste Form Production by Hot Isostatic Pressing, FCRD-MRWFD-2016-000267, ORNL/SR-2016/759, Oak Ridge National Laboratory, Oak Ridge, TN (2017). https://doi.org/10.2172/1414720

[24] R.T. Jubin, S.H. Bruffey, and K.K. Patton, Expanded Analysis of Hot Isostatic Pressed Iodine-Loaded Silver-Exchanged Mordenite, FCRD-SWF-2014-000278; ORNL/LTR-2014/476, Oak Ridge National Laboratory, Oak Ridge, TN (2014). https://doi.org/10.2172/1160345

[25] S.H. Bruffey and R.T. Jubin, Preparation of Four Large-format Hot Isostatically Pressed I-AgZ Waste Form Samples for Performance Testing, NTRD-MRWFD-2018-000198; ORNL/SPR-2018/1026, Oak Ridge National Laboratory, Oak Ridge, TN (2018). https://doi.org/10.2172/1506807

[26] S.H. Bruffey and R.T. Jubin, Recommend HIP Conditions for AgZ, FCRD-MRWFD-2015-000423, ORNL/SPR-2015/503, Oak Ridge National Laboratory, Oak Ridge, TN. (2015). https://doi.org/10.2172/1239759

[27] E.R. Maddrell, E.R. Vance, and D.J. Gregg, Capture of iodine from the vapour phase and immobilisation as sodalite, J. Nucl. Mater., 467 (2015) 271-279. http://dx.doi.org/10.1016/j.jnucmat.2015.09.038

[28] E.R. Vance, D.J. Gregg, C. Grant, A. Stopic, and E.R. Maddrell, Silver iodide sodalite for ^{129}I immobilisation, J. Nucl. Mater., 480 (2016) 177-181. http://dx.doi.org/10.1016/j.jnucmat.2016.08.013

[29] J. Nam, S. Chong, B.J. Riley, and J.S. McCloy, Iodosodalite Waste Forms from Low-Temperature Aqueous Process, MRS Adv., 3 (2018) 1093-1103. https://doi.org/10.1557/adv.2018.225

[30] D.L. Bollinger, J. Erickson, J.M. Bussey, and J.S. McCloy, Process optimization of caustic scrubber and iodine-129 immobilization in sodalite-based waste forms, MRS Adv., 7 (2022) 110-116. https://doi.org/10.1557/s43580-022-00229-y

[31] A.J. Lere-Adams, N. Stone-Weiss, D.L. Bollinger, and J.S. McCloy, Scoping studies for low-temperature melting ZnO–Bi_2O_3–(B_2O_3, SiO_2) binder glass, MRS Adv., 7 (2022) 90-94. https://doi.org/10.1557/s43580-022-00219-0

[32] B.J. Riley, J.D. Vienna, S.M. Frank, J.O. Kroll, J.A. Peterson, N.L. Canfield, Z. Zhu, J. Zhang, K. Kruska, D.K. Schreiber, and J.V. Crum, Glass binder development for a glass-bonded sodalite ceramic waste form, J. Nucl. Mater., 489 (2017) 42-63. https://doi.org/10.1016/j.jnucmat.2017.03.041

[33] ASTM, Standard Test Method for Accelerated Leach Test for Measuring Contaminant Releases from Solid Waste, ASTM Committee C26 on Nuclear Fuel Cycle, (2021).

[34] J.-C. Buhl, Kinetics and mechanism of the intra-cage oxidation of nitrite sodalite, React. Kin. Catal. Lett., 43 (1991) 577-582. https://doi.org/10.1007/BF02064731

[35] C.M. Schwarz, M. Kang, Q. Altemose, K. Raichle, B. Schnable, C. Grabill, J. Rice, M. Truman, C. Pantano, and I. Mingareev, Processing and properties of novel ZnO–Bi_2O_3–B_2O_3 glass-ceramic nanocomposites, J. Alloys Comp., 820 (2020) 153173. https://doi.org/10.1016/j.jallcom.2019.153173

[36] Q. Wen, W. Cheng, M. Yan, Y. Liu, Z. Zhang, Y. Xie, D. Shao, and X. Lu, Bismuth coordinates with iodine atoms to form chemical bonds for existing stabilization in boron glass, Inorg. Chem., 61 (2022) 9860-9867. https://doi.org/10.1021/acs.inorgchem.1c03680

[37] E. Maddrell, E. Vance, and D. Gregg, Capture of iodine from the vapour phase and immobilisation as sodalite, J. Nucl. Mater., 467 (2015) 271-279. https://doi.org/10.1016/j.jnucmat.2015.09.038

[38] E. Maddrell, E. Vance, C. Grant, Z. Aly, A. Stopic, T. Palmer, J. Harrison, and D. Gregg, Silver iodide sodalite–Wasteform/Hip canister interactions and aqueous durability, J. Nucl. Mater., 517 (2019) 71-79. https://doi.org/10.1016/j.jnucmat.2019.02.002

[39] I. Padilla, A. López-Delgado, and M. Romero, Kinetic study of the transformation of sodalite to nepheline, J. Am. Ceram. Soc., 105 (2022) 4336-4347. https://dx.doi.org/10.1111/jace.18365

[40] S. Khajavi, S. Sartipi, J. Gascon, J.C. Jansen, and F. Kapteijn, Thermostability of hydroxy sodalite in view of membrane applications, Microp. Mesop. Mater., 132 (2010) 510-517. https://doi.org/10.1016/j.micromeso.2010.03.035

[41] S. Cartlidge and W.M. Meier, Solid state transformations of synthetic CHA-and EAB-type zeolites in the sodium form, Zeolites, 4 (1984) 218-225. https://doi.org/10.1016/0144-2449(84)90027-7

[42] Q. Xian, X. Xiao, J. Yu, Y. Gan, L. Chen, X. He, E. Wang, H. Dan, L. Zhu, Y. Ding, and T. Duan, High Retention Immobilization of Iodine in B–Bi–Zn Oxide Glass Using Bi_2O_3 as a Stabilizer under a N_2 Atmosphere, Inorg. Chem., 61 (2022) 19633-19641. https://doi.org/10.1021/acs.inorgchem.2c03601

[43] G. Wei, X. Shu, Z. Zhang, Q. Li, Y. Liu, X. Wang, Y. Xie, B. Li, D. Shao, and X. Lu, B_2O_3–Bi_2O_3–ZnO based materials for low-sintering temperature immobilization of iodine adsorbed waste, J. Solid State Chem., 2020) 121518. https://doi.org/10.1016/j.jssc.2020.121518